Effects of ionization in single-bubble sonoluminescence

C. Y. Ho,[1] L. Yuan,[2] M.-C. Chu,[1] P. T. Leung,[1] and W. Wei[3]
[1]*Department of Physics, The Chinese University of Hong Kong, Shatin, N.T., Hong Kong*
[2]*LSEC and Institute of Computational Mathematics, Academy of Mathematics and System Sciences, Academia Sinica, Beijing 100080, People's Republic of China*
[3]*Nonlinear Center, University of Science and Technology of China, Hefei 230026, People's Republic of China*
(Received 6 September 2001; published 15 March 2002)

We studied the effects of ionization in a sonoluminescing (SL) bubble within the hydrodynamic framework. The thermodynamic variables and the degrees of ionization inside the bubble throughout an oscillation cycle are obtained by solving the hydrodynamic equations assuming spherical symmetry. Several models are used to compute the emitted radiation, which are then compared with experimental data. Numerical results show that shock waves are absent in the stable SL regime, and compressional waves are already strong enough to produce moderate temperature and ionization. The degrees of ionization at the bubble center are found to be within 7% to 30%, and Ar^+ is the only dominant ion. Moreover, an opacity-corrected blackbody radiation model gives the peak power, pulse widths, and spectra that agree very well with the experimental data.

DOI: 10.1103/PhysRevE.65.041201 PACS number(s): 78.60.Mq, 47.40.−x, 52.50.Lp, 43.25.+y

I. INTRODUCTION

The remarkable discovery that acoustic energy can be converted to light through an oscillating air bubble trapped in water has triggered widespread interest in single-bubble sonoluminescence (SBSL) [1]. Under certain conditions, a narrow and regular flash of blue-white light with a width of about 40–350 ps is emitted in each cycle of the bubble oscillation during the strong collapse of the bubble [2–4]. The bubble can oscillate synchronously and stably for a few days through billions of acoustic cycles. Moreover, such a conversion of sound into light represents a high concentration of energy by 12 orders of magnitude.

The mechanism of SBSL light emission is still under debate. A number of models were proposed to explain the cause of light emission, which include blackbody radiation [5], shock wave model [6–10], collision-induced emission [11,12], quantum vacuum radiation [13], confined-electron model [14], and even fusion [8].

Previous hydrodynamic calculations have presented rather contradictory pictures of the bubble interior during light emission. On the one hand, calculations based on inviscid spherical hydrodynamics [7–9] suggested that a converging shock produced high temperature and pressure and the reflected diverging shock quenched them in picosecond time scale [8–10,6]. Xu *et al.* reported very strong multiple ionizations, up to Ar^{5+}, based on this scenario [15,16]. This model could explain the emergence of a picosecond time scale as well as the large energy concentration. But the effects of transport processes, surface tension, the equation of state (EOS), and the compressibility of liquid were also largely ignored. One recent calculation that includes a temperature-dependent surface tension and thermal conduction shows that most of the trends of experimental data can be explained based on a shock-induced cool dense plasma model [10]. On the other hand, assuming a uniform bubble interior, which therefore leads to a considerably lower maximum temperature, Hilgenfeldt *et al.* could explain the SL spectral shape and the wavelength independence of the pulse widths using a modified blackbody radiation model accounting for the small emissivity and absorption of a weakly ionized gas [17]. However, the assumed uniformity of the bubble content is unrealistic given the rapid collapse of the bubble around the short duration of light emission.

The validity of most of these models depends on the details of the hydrothermal processes inside the bubble, and therefore a realistic hydrodynamic model is essential. Recent studies [18–22] that include parts or all of the effects of the transport processes demonstrate that the shock wave is not essential for stable SBSL. Rather, a smooth compressional wave emerges naturally in a collapsing bubble, and a large fraction of the bubble content is heated to moderate temperatures for a short duration. Nevertheless, the predicted temperature is of several 10^4 K and can indeed induce chemical reactions and ionization.

We study in this paper the degrees of ionization occurring at the SBSL conditions and their relevance to the light-emission mechanism of SBSL based on a realistic hydrodynamic calculation. Our major conclusions are: (1) shock waves are absent in the stable SBSL regime; (2) the degrees of ionization are found to be within 7 to 30 %, and Ar^+ is the only dominant ion; (3) with this moderate ionization, the bubble becomes optically opaque, and a refined blackbody radiation model taking into account the opacity and absorption of the bubble content gives the peak power, pulse widths, and spectra that fit the experimental data very well.

II. HYDRODYNAMIC MODELS

In this section, we extend a hydrodynamical framework by Yuan *et al.* and Cheng *et al.* [21,22] to include the calculation of ionization and recombination processes. In the model, the Navier-Stokes (NS) equations are coupled to the Rayleigh-Plesset (RP) equation which describes the bubble-wall motion. The energy equation for the surrounding water is also solved at the same time. The effects of viscosity, surface tension, equation of state (EOS), and the compressibility of liquid are taken in account.

A. RP equation for bubble-wall motion

For a spherical bubble in liquid, the equation for the bubble-wall motion was formulated by Rayleigh [23] in 1917 and modified by Plesset [24], and Noltingk and Neppiras [5] in 1950. The equation is called the Rayleigh-Plesset (RP) equation.

Several forms of the RP equation have been used in the literature, which differ in the terms that account for the compressibility of the liquid surrounding the bubble, characterized by the bubble-wall Mach number $M \equiv \dot{R}/c_l$, where c_l is the speed of sound in the liquid. It has been shown that whether shocks emerge depends strongly on the form of the RP equation [21,22]. An SL bubble undergoes an enormous compression; the surrounding liquid should also be greatly compressed, and hence the speed of sound in the liquid varies during a SL cycle. To account for the effect of the liquid compressibility better, we use a more complete RP equation that includes terms to first order in M and allows for a variable c_l [25], giving

$$\frac{1-M}{1+M}R\ddot{R}+\frac{3-M}{2(1+M)}\dot{R}^2=H_b-\frac{P_s(t')}{\rho_\infty}+\frac{t_R\dot{H}_b}{1+M}. \quad (1)$$

Here overdots denote time derivatives, $t_R \equiv R/c_l$, $t' \equiv t+t_R$, ρ_∞ is the ambient density, $P_s(t')=-P_a \sin(\omega t')$ is the pressure of the sound field with frequency ω and amplitude P_a. The enthalpies of the liquid H_l and c_l are given by

$$H_l=\int_{P_\infty}^{P_l}\frac{dP}{\rho}, \quad c_l^2=\frac{dP}{d\rho}. \quad (2)$$

For water, c_l and H_l are obtained using an equation of state of the modified Tait form [26]

$$\frac{P+B}{P_\infty+B}=\left(\frac{\rho}{\rho_\infty}\right)^n, \quad (3)$$

where $B=3049.13$ bar and $n=7.15$. Combining Eqs. (2) and (3), we get

$$H_l=\frac{n}{n-1}\left(\frac{P_l+B}{\rho}-\frac{P_\infty+B}{\rho_\infty}\right), \quad c_l^2=\frac{n(P_l+B)}{\rho}. \quad (4)$$

In computing H_l and c_l, the pressure $P_l(t)$ on the liquid side of the gas-liquid interface is related to the pressure $P_g(R,t)$ on the gas side of the gas-liquid interface by

$$P_g(R,t)-\tau_{rr}|_{r=R}=P_l(t)+\frac{4\eta\dot{R}}{R}+\frac{2\sigma}{R}, \quad (5)$$

which states that the pressure on the gas side differs from that on the liquid side due to the effects of surface tension and the normal component of viscous stresses [26].

Equation (1) is used for most of our simulations. To be consistent with Ref. [21], Eq. (1) is labeled as RP3. Another form of the RP-type equation will also be used as a comparison, in which the liquid is taken to be incompressible and the Mach number is kept only to the zeroth-order term

$$R\ddot{R}+\frac{3}{2}\dot{R}^2=\frac{1}{\rho_\infty}[P_l-P_s(t)-P_\infty]+\frac{R}{\rho_\infty c_\infty}\frac{d}{dt}[P_l-P_s(t)], \quad (6)$$

which is labeled as RP1.

B. Conservation equations for gas in bubble

Neglecting mass diffusion, which is a much slower process [27], the dynamics of the gas inside a spherical bubble is described by the compressible NS equations, which represent the conservation of mass, momentum, and energy. They can be written into a conservative form with source terms

$$\frac{\partial\rho}{\partial t}+\frac{\partial}{\partial r}(\rho v)=-\frac{2\rho v}{r}, \quad (7)$$

$$\frac{\partial(\rho v)}{\partial t}+\frac{\partial}{\partial r}(\rho v^2+P)=-\frac{2\rho v^2}{r}+\frac{1}{r^2}\frac{\partial}{\partial r}(r^2\tau_{rr})+\frac{\tau_{rr}}{r}, \quad (8)$$

$$\frac{\partial(\rho E)}{\partial t}+\frac{\partial}{\partial r}(\rho E+P)v=-\frac{2(\rho E+P)v}{r}+\frac{1}{r^2}\frac{\partial}{\partial r}\left[r^2\left(v\tau_{rr}+k\frac{\partial T}{\partial r}\right)\right]. \quad (9)$$

Here $E=e+v^2/2$ is the total energy per unit mass, r, ρ, v, P, T, τ_{rr}, k, and e are the radial distance from the center of the bubble, gas density, radial velocity, pressure, temperature, normal viscous stress, coefficient of thermal conductivity, and internal energy per unit mass, respectively. If we are dealing with inviscid flow, the last two terms in Eq. (8) and the last term in Eq. (9) should be ignored, and the resulting equations are called the Euler equations.

In order to keep track of the densities of the N_s species, N_s-1 more species conservation equations are required in addition to Eqs. (7)–(9). The ion densities change due to ionization and recombination, and so source terms must be added to the right-hand side of the species conservation equations. The maximum ionization level is taken to be five, which should be adequate for the present temperature range. Our results indicate that even the second ionization level can be safely ignored in practice.

For convenience, let f_j be the mass fraction of Ar^{j+} (with $j=0,1,2,3,4,5$) or electron (with $j=e$). Therefore ρf_j represents the mass density of an individual species, and the number density of an individual species is related to its mass fraction by $n_j=\rho f_j/m_j$, where m_j is the mass of an atom (for $j=0$), or an ion with a charge j (for $j=1-5$), or an electron (for $j=e$). The mass fraction of Ar^{5+} can be found by $f_5=1-f_e-\Sigma_{j=0}^{4}f_j$. The species mass conservation equations is given by

$$\frac{\partial(\rho f_j)}{\partial t}+\frac{\partial}{\partial r}(\rho f_j v)=-\frac{2\rho f_j v}{r}+(S_s)_j. \tag{10}$$

Here, the extra term $(S_s)_j$ is the source term for ρf_j arising from ionization and recombination processes. The source term $(S_s)_j$ depends on the net rate of change of the number density of the species $\dot{n}_j$ by

$$(S_s)_j=m_j\dot{n}_j. \tag{11}$$

In this case, the rate of change of n_j is determined by the ionization and recombination processes. Therefore, for the ions ($j=0,1,2,3,4,5$), the net rate of change is given by

$$\dot{n}_j=n_{j-1}n_e\alpha^{\text{ion}}_{j-1\to j}-n_jn_e\alpha^{\text{ion}}_{j\to j+1}+n_{j+1}n_e(\alpha^{\text{rrec}}_{j+1\to j}+\alpha^{\text{trec}}_{j+1\to j})-n_jn_e(\alpha^{\text{rrec}}_{j\to j-1}+\alpha^{\text{trec}}_{j\to j-1}). \tag{12}$$

Here $\alpha^{\text{ion}}_{j\to j+1}$, $\alpha^{\text{rrec}}_{j\to j-1}$, and $\alpha^{\text{trec}}_{j\to j-1}$ denote the rates of ionization, radiative recombination, and three-body recombination of particles with a charge of j. The formulas for them are given in [16].

The net rate of change of the number density of electrons is simply given by charge conservation. Knowing that

$$f_e=1-\sum_{j=0}^{5}f_j, \tag{13}$$

we take the time derivative and multiply both sides by ρ to obtain

$$(S_s)_e=-\sum_{j=0}^{5}(S_s)_j. \tag{14}$$

C. Equation of state

The hydrodynamics of the bubble is affected by the EOS. The most widely used van der Waals EOS can be modified to take into account the ionization processes [15]

$$p=\left(\sum_{j=0}^{5}\frac{f_j}{m_j}+\frac{f_e}{m_e}\right)\frac{k_B\rho T}{1-b\rho},$$

$$e=\frac{3}{2}k_BT\left(\sum_{j=0}^{5}\frac{f_j}{m_j}+\frac{f_e}{m_e}\right)+k_B\sum_{j=1}^{5}\sum_{i=j}^{5}\frac{f_i}{m_i}T_j, \tag{15}$$

where T_j is the ionization energy of an ion with charge $j-1$, and b is the excluded volume. Therefore, $\rho f_j/m_j$ gives the number density n_j of Ar^{j+}, and $\rho f_e/m_e$ gives the number density of electron n_e. We denote this EOS by MVEOS.

The physical meanings of Eqs. (15) are clear. The pressure contributed by different species are taken into account separately in proportion to their abundance. The internal energy of the gas e consists of both the thermal energy and ionization energy. The first term in the right-hand side of e represents the thermal energy of the gas, while the second term represents the total energy required for ionization. Note that the EOS itself is thermally inconsistent.

A more realistic EOS for argon has been adopted in recent studies [19,22]. Here we modify this EOS by taking into account the ionization processes and denote it MYEOS. The EOS is constructed so that the pressure p and internal energy e can be decomposed into three parts: (1) the zero-temperature part p_c, e_c, (2) the nuclear motion part p_n, e_n, and (3) the electron motion part p_e, e_e,

$$p(\rho,T,\mathbf{f})=p_c(\rho)+p_n(\rho,T,\mathbf{f})+p_e(\rho,T,\mathbf{f}),$$

$$e(\rho,T,\mathbf{f})=e_c(\rho)+e_n(\rho,T,\mathbf{f})+e_e(\rho,T,\mathbf{f}). \tag{16}$$

The zero-temperature part is exactly the same as that in Ref. [19]. The nuclear motion part includes the ideal gas contribution and a configurational soft-sphere piece that represents the nonideal behavior of the dense fluid,

$$p_n=k_B\rho T\sum_{j=0}^{5}\frac{f_j}{m_j}+\frac{1}{18}k_B\rho Tqj_n(j_n+4)\,\eta^{j_n/9}\tau^{1/3}\sum_{j=0}^{5}\frac{f_j}{m_j},$$

$$e_n=\frac{3}{2}k_BT\sum_{j=0}^{5}\frac{f_j}{m_j}+\frac{1}{6}k_BTq(j_n+4)\,\eta^{j_n/9}\tau^{1/3}\sum_{j=0}^{5}\frac{f_j}{m_j}, \tag{17}$$

where $\tau=T_1/T$, T_1 is a reference temperature set as 1 eV, and $\eta=\rho/\rho_0$, with ρ_0 the density of the cold solid at $p=0$. The parameters q and j_n are fitted to be 0.2 and 6, respectively [19].

The electrons are treated as ideal gas particles so that the electron pressure and energy are

$$p_e=\frac{f_e}{m_e}k_B\rho T,\quad e_e=\frac{3}{2}\frac{f_e}{m_e}k_BT+k_B\sum_{j=1}^{L}\sum_{i=j}^{L}\frac{f_i}{m_i}T_j. \tag{18}$$

D. Energy equation in liquid

To include the heat transfer between the bubble and the surrounding water, the energy equation for the water is also needed

$$\frac{\partial T_l}{\partial t}+v_l\frac{\partial T_l}{\partial r}=D_l\frac{1}{r^2}\frac{\partial}{\partial r}\left(r^2\frac{\partial T_l}{\partial r}\right), \tag{19}$$

where T_l, v_l, and D_l are the temperature, velocity and the thermal diffusion coefficient of the liquid.

E. Photon absorption due to ionized gas

Since the gas is ionized, the ions and electrons will interact with photons. Photons can be absorbed by free electrons, with an ion acting as a third partner to conserve energy and momentum. The process is called the free-free absorption of light by ions. Since Ar^+ is the dominant ion in the bubble, we will only take into account the absorption by Ar^+. The absorption coefficient $\kappa_\lambda^{\text{ff}+}$ is given by [28]

$$\kappa_\lambda^{\mathrm{ff}+}=\frac{4}{3}\left(\frac{2\pi}{3m_e k_B T}\right)^{1/2}\frac{e^6\lambda^3}{(4\pi\epsilon_0)^3 hc^4 m_e}n_1 n_e, \qquad (20)$$

where n_1 is the number density of Ar^+ and ϵ_0 is the vacuum permeability.

Photons can also be absorbed by free electrons with a neutral atom as a third partner. The process is called the free-free absorption of light by atoms. The absorption coefficient $\kappa_\lambda^{\mathrm{ff0}}$ is obtained as a function of the temperature and number densities of neutral atoms and electrons

$$\kappa_\lambda^{\mathrm{ff0}}=\frac{e^2\lambda^2}{(4\pi\epsilon_0)\pi c^3}\times 4\pi\left(\frac{2k_B T}{\pi m_e}\right)^{3/2}\left(c_{tr}+\frac{d_{tr}}{3k_B T}\right)n_0 n_e, \qquad (21)$$

where $c_{\mathrm{tr}}\approx 1.6\times 10^{-20}$ m^2/eV, $d_{\mathrm{tr}}\approx -0.6\times 10^{-20}$ m^2, v_e is the velocity of the interacting electrons, and n_0 is the number density of the neutral atoms.

Finally, a photon can be absorbed by the transition of an electron into the continuous energy spectrum. The corresponding absorption coefficient is given by [29]

$$\kappa_\lambda^{\mathrm{bf}}=\frac{32\pi^4}{3\sqrt{3}}\frac{e^{10}m_e n_0}{(4\pi\epsilon_0)^5 h^6 c^4}\frac{k_B T}{E_{\mathrm{ion}}}\lambda^3\exp\left(-\frac{E_{\mathrm{ion}}}{k_B T}\right)\times\left[\exp\left(\frac{hc/\lambda}{k_B T}\right)-1\right]. \qquad (22)$$

We sum over the above three absorption coefficients to obtain the overall absorption coefficient $\kappa_\lambda^{\mathrm{tot}}$,

$$\kappa_\lambda^{\mathrm{tot}}=\kappa_\lambda^{\mathrm{ff}+}+\kappa_\lambda^{\mathrm{ff0}}+\kappa_\lambda^{\mathrm{bf}}. \qquad (23)$$

F. Power radiated by bubble

We calculate the emitted light spectrum using a blackbody radiation model refined in two ways to accommodate the effects of ionization [30]. First, the presence of ionized plasma in the core of an SL bubble greatly reduces the photon mean free path, and hence we divide the bubble into a strongly absorbing core and a weakly absorbing outershell, according to the calculated mean free path, which is also wavelength dependent. We define the radius of the ''black'' core R_c to be the point where the mean free path $l(r,t,\lambda)$ equals a fraction of the bubble radius, $l(R_c,t,\lambda)=R(t)/n_{\mathrm{co}}$. Furthermore, we define an *inner* core whose radius R_{ci} is related to the bubble radius in a similar manner: $l(R_{\mathrm{ci}},t,\lambda)=R(t)/n_{\mathrm{ci}}$, with $n_{\mathrm{ci}}>n_{\mathrm{co}}$. The surface temperature of the core $T(r=R_c)$ is increased because photons emitted in the inner core are absorbed by the surface layer of the core. We treat this effect approximately by redistributing the radiation energy of the *inner* core to the gas in the surface layer $R_{\mathrm{ci}}<r<R_c$. In practice, we choose n_{ci}, n_{co} to be eight and four, respectively, but our results are hardly changed if they are chosen to be ten and five instead. Note that the size of the core and the mean free paths are smaller than the wavelengths of the emitted light. A careful investigation of the possible intricate effects this may cause is certainly interesting, and we have considered them in a recent paper for a static bubble [31]. However, it is beyond the scope of the present paper to incorporate these finite-size effects into the case of a rapidly oscillating bubble.

Due to the short mean free path in the ''black'' inner core, we assume that light traversing through the core is completely absorbed. Therefore, light can only be emitted outward from the surface of the core. We also assume that photons emitted from the outer shell passing through the core is completely blocked, which we account for by introducing a correction factor

$$\Theta(r)=\frac{1}{2}\left[1+\frac{\sqrt{r^2-R_c^2}}{r}\right]. \qquad (24)$$

Second, in the ''gray'' outershell, the *surface* emission from the ''black'' core is further subjected to the absorption effect of the ''gray'' outershell, as described by a damped intensity in the small-opacity approximation [29]. The emitted intensity therefore decreases along the path by the exponential of the absorption coefficient integrated along the path

$$I(r)=I(r_0)\exp\left(-\int_{r_0}^{R}\kappa_\lambda^{\mathrm{tot}}(r')dr'\right), \qquad (25)$$

where r_0 is the emission point, which can be either from the surface of the black core or within the gray shell, and R is the bubble radius.

By putting Eqs. (24)–(25) together and integrating over the whole bubble, we obtain the total spectral radiance (power emitted per wavelength interval) of the bubble content at wavelength λ to be

$$P_\lambda^{\mathrm{Pl}}(t)=\int_{R_c}^{R}16\pi\kappa_\lambda^{\mathrm{tot}}(r,t)R_\lambda^{\mathrm{Pl}}(r,t)\times\exp\left(-\int_{r}^{R}\kappa_\lambda^{\mathrm{tot}}(r')dr'\right)\Theta(r)r^2dr+4\pi R_c^2 R_\lambda^{\mathrm{Pl}}(R_c,t)\exp\left(-\int_{R_c}^{R}\kappa_\lambda^{\mathrm{tot}}(r')dr'\right), \qquad (26)$$

where

$$R_\lambda^{\mathrm{Pl}}[T(r,t)]=\frac{2\pi hc^2}{\lambda^5}\frac{1}{\exp(hc/\lambda k_B T)-1} \qquad (27)$$

is the spectral emissive power, and the overall absorption coefficient $\kappa_\lambda^{\mathrm{tot}}$ is wavelength dependent and is greater for red light than for UV.

G. Choice of R_0 and physical parameters

The value of the ambient bubble radius R_0 is determined by experimentally controllable parameters, such as the driving pressure, the water temperature, the gas concentration in water, etc. Experimental results have shown that a change of only 20% in the bubble radius is associated with a factor of

200 change in the intensity of the emitted light [32]. Therefore, we should choose the values of the ambient radius carefully. Stable and stationary values for the ambient radius R_0 can be predicted by considering stable mass diffusive equilibrium [33,34]. We simply use the values of R_0 from Ref. [28] based on the calculation of diffusive equilibrium for the driving frequency $f=20$ kHz with water temperature 293 K at dissolved gas concentrations $c_\infty/c_0=0.20\%$. We choose $P_a=1.275$, 1.3, 1.325, and 1.35 atm and $R_0=2.6$, 4, 4.7, and 5.4 μm, respectively. We use standard values of the material constants: $P_\infty=101\,325$ Pa, $\eta=1.01\times10^{-3}$ kg m^{-1} s^{-1}, $c_{l\infty}=1483$ m s^{-1}, $\rho_l=998$ kg m^{-3}, $\sigma=0.0728$ kg s^{-2}, $k_l=0.609$ W m^{-1} K^{-1}, and $c_{p,l}=4179$ J kg^{-1} K^{-1}.

III. NUMERICAL METHODS

Before we solve the whole set of governing equations, we use $x\equiv r/R(t)$ to transform the gas dynamics equations Eqs. (7)–(10) to a fixed coordinate $x\subset[0,1]$. The resulting equations are

$$\frac{\partial \mathbf{Q}}{\partial t}+\frac{\partial \mathbf{F}(\mathbf{Q})}{\partial x}=\mathbf{H}(\mathbf{Q})+\mathbf{F}_v(\mathbf{Q})+\mathbf{S}_s(\mathbf{Q}). \tag{28}$$

Here $\mathbf{Q}=R(\rho\mathbf{f},\rho,\rho v,\rho E)^T$. The inviscid fluxes are $\mathbf{F}=(\rho\mathbf{f}(v-x\dot{R}),\rho(v-x\dot{R}),\rho v^2+p-\rho v x\dot{R},(\rho E+p)v-\rho E x\dot{R})^T$, and the spherical sources are $\mathbf{H}=-2v(\rho\mathbf{f},\rho,\rho v,(\rho E+p))^T/x$. The diffusive transport terms are given by $\mathbf{F}_v=(0,0,\partial_x(x^2\tau_{rr})+x\tau_{rr},\partial_x[x^2(v\tau_{rr}+\kappa\partial_x T/R])^T/x^2$, where $\tau_{rr}=4\mu(\partial_x v-v/x)/3R$ is the normal viscous stress, κ is the coefficient of thermal conductivity, μ is the dynamic viscosity. The source term $\mathbf{S}_s$ accounts for the mass production due to ionization and recombination processes.

We apply a second-order total-variational-diminishing (TVD) scheme [35] to the inviscid flux terms of Eq. (28), with a simple arithmetic average of the interface variables [36]. We treat the terms in the right-hand side of Eq. (28) explicitly. Details of the scheme can be found in Ref. [21]. We use 400 grid points for the NS equations in the bubble and 80 points for the water temperature equation. We employ the RP solution alone assuming isothermal and uniform gas distribution up to the point where $R=3R_0$ prior to the main collapse. We then switch to the solution of the full hydrodynamic equations. The initial number densities of ions and electrons are estimated using the Saha equation [29]. Both the MVEOS and MYEOS can be adopted.

IV. NUMERICAL RESULTS

A. Effects of ionization on hydrodynamic variables

In Figs. 1(a) and 1(b), we show snapshots of the spatial profiles of several thermodynamic variables around the moment of minimum bubble radius for the case with $P_a=1.325$ atm and $R_0=4.7$ μm. Such a combination of the driving pressure and ambient radius represents a typical condition of stable SBSL. Six profiles are shown in Fig. 1(a), corresponding to 68 ps (t1), 51 ps (t2), 37 ps (t3), 25 ps (t4), 14 ps (t5), 3 ps (t6) *before* the moment of minimum bubble radius, whereas the six shown in Fig. 1(b) correspond to 7 ps (t7), 17 ps (t8), 27 ps (t9), 38 ps (t10), 50 ps (t11), and 65 ps (t12) *after*. It can be seen in Fig. 1(a) that the contraction of the bubble between t1 and t4 results in a rapid increase in the temperature, pressure, and density near the bubble center. However, the enormous buildup of the density and pressure (up to 0.7 g/cc and 3×10^5 atm, respectively) at the bubble center begins to reverse the inward collapse at small r starting at t4. Between t4 and t8, materials near the bubble center expand *outward* while the outer layer of the bubble continues to contract *inward*. As a result, a small layer of gas is compressed, shown as small bumps in the density and pressure profiles, and this ''compressional wave'' moves inward between t4 and t8. Upon reaching the center at t9, the compressional wave produces a surge in temperature, pressure, and

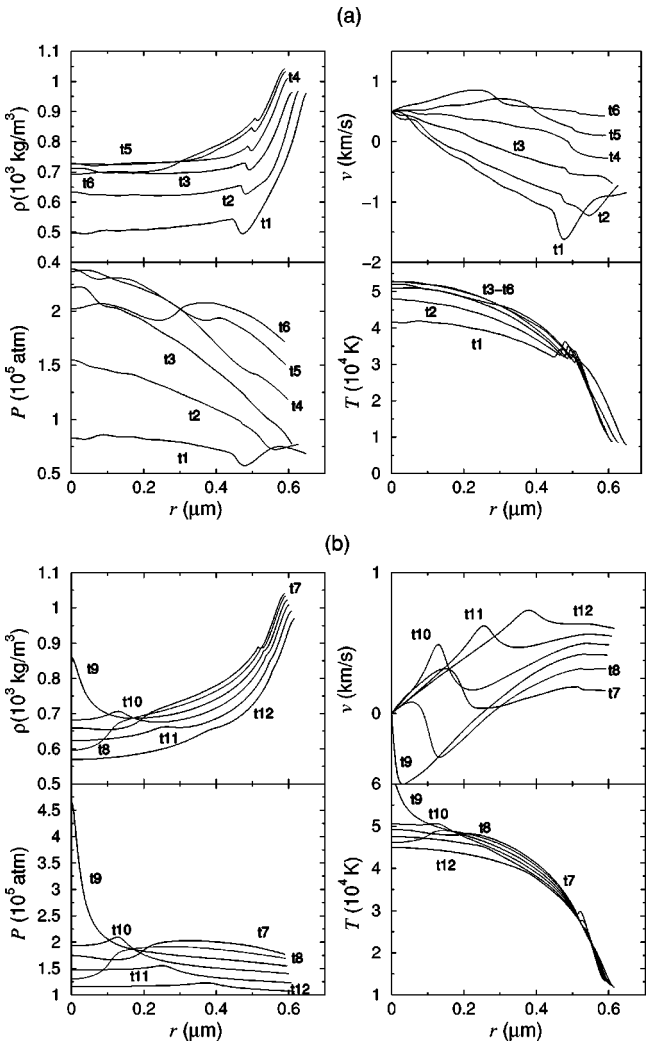

FIG. 1. Snapshots of the spatial profiles of density, velocity, pressure, and temperature for $P_a=1.325$ atm and $R_0=4.7$ μm using MVEOS and RP3. Here, t1$=-68$ ps, t2$=-51$ ps, t3$=-37$ ps, t4$=-25$ ps, t5$=-14$ ps, t6$=-3$ ps, t7$=7$ ps, t8$=17$ ps, t9$=27$ ps, t10$=38$ ps, t11$=50$ ps, and t12$=65$ ps, where $t=0$ is the time that the bubble attains its minimum radius. (a) and (b) show the evolution from t1 (t7) until t6 (t12).

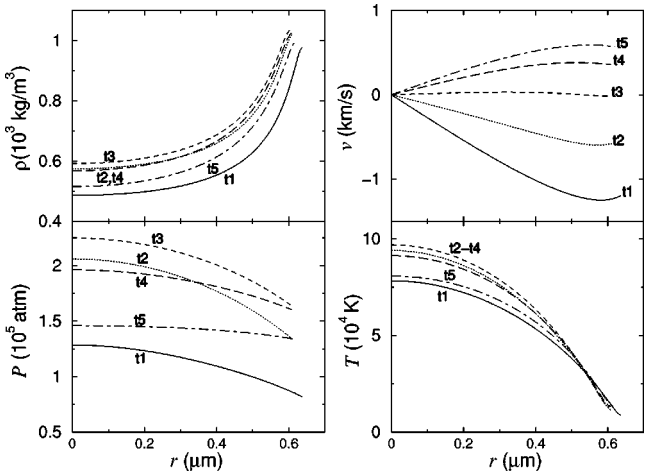

FIG. 2. Same as Fig. 1, but using VEOS and without considering ionization. Here, t1 = −52 ps, t2 = −24 ps, t3 = −1 ps, t4 = 20 ps, and t5 = 44 ps.

density for a brief moment (of less than 10 ps), and it is then reflected from the bubble center and moves outward between t9 and t12.

Similar profiles are shown in Fig. 2 using the Van der Waals EOS without considering ionization. The velocity is approximately linear in r and the pressure is nearly uniform, while a boundary layer shows up near the bubble wall for both the density and temperature. Comparison of Figs. 1 and 2 shows that ionization tends to lower the temperature and hence the speed of sound in the gas, which in turn leads to a steepening of the compressional waves.

We show in Fig. 3 the spatial profiles (solid lines) of the density fractions, f_1 and f_2, of the Ar^+ and Ar^{2+} ion species in the bubble around the instant of maximum compression. The ionized core is quite wide with a radius extending to

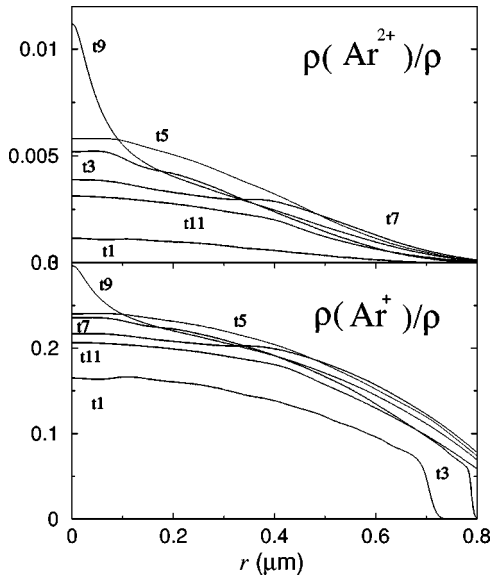

FIG. 3. Snapshots of the spatial profiles of the density fractions of Ar^+ and Ar^{2+} for $P_a = 1.325$ atm and $R_0 = 4.7$ μm using MVEOS and RP3. The values of t1, t3, etc., are the same as those in Fig. 1.

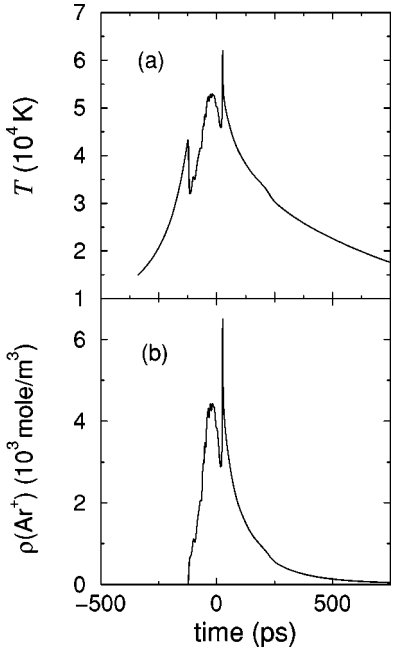

FIG. 4. The time variations of (a) the temperature, (b) the number density of Ar^+ at the bubble center for $P_a = 1.325$ atm and $R_0 = 4.7$ μm using MVEOS and RP3. Here, the bubble attains its minimum radius at $t = 0$.

about 90% of the bubble radius. We found that Ar^+ is the only dominant ion (at most about 30% as shown) with very few Ar^{2+} present (below 1%); higher ionization states are virtually absent. This is in stark contrast to the strong multiple ionizations reported in an earlier work by Xu *et al.* [15], based on inviscid hydrodynamics ignoring effects of heat transport, surface tension, and the compressibility of the surrounding liquid. On the other hand, the degrees of ionization we found here are much higher than those (below 1%) reported in Refs. [17,28], which assumes a uniform interior of the bubble.

B. Time variation of temperature

As shown in Fig. 4(a), the central temperature increases at first. The number density of Ar^+ at the bubble center is shown in Fig. 4(b), and we found that there is no ionization at that time. At about $t = -125$ ps, the central temperature suddenly drops from about 43 000 K to about 32 000 K, and ionization starts at the same time.

The temperature and the Ar^+ density continue to rise after $t = -125$ ps, and they reach the local maximum slightly before the time that the bubble attains its minimum radius ($t = 0$ ps). Numerical results also show that there is a sudden increase in the temperature and the Ar^+ density around $t = 17$ ps (t9 in Figs. 1 and 3), corresponding to the convergence of the compressional wave to the center of the bubble, which lasts for a very short duration only.

C. Near upper threshold of SBSL

According to Ref. [28], the parametric surface instability restricts the ambient radius to less than about 5.5 μm. Be-

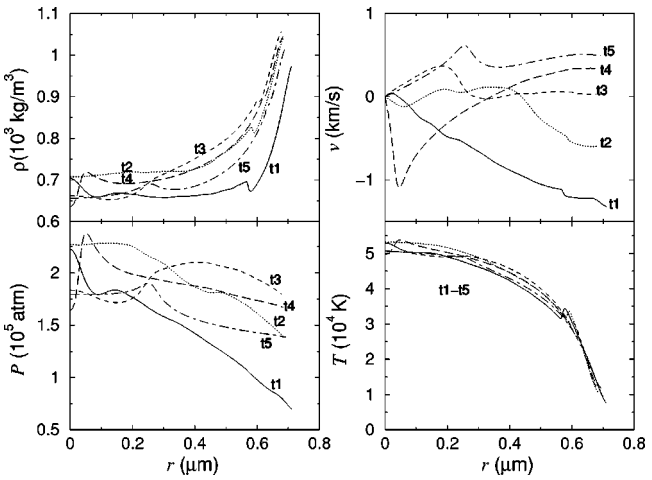

FIG. 5. Same as Fig. 1, but with $P_a=1.35$ atm and $R_0=5.4$ μm. Here, t1$=-50$ ps, t2$=-22$ ps, t3$=1$ ps, t4 $=24$ ps, and t5$=47$ ps.

yond this radius, the bubble becomes unstable, and it will either shrink or burst after a short time. Here we discuss what happens near the upper threshold of SBSL. The conditions used are: driving frequency $f=20$ kHz, driving pressure $P_a=1.35$ atm, and $R_0=5.4$ μm.

We show in Fig. 5 snapshots of the spatial profiles of several thermodynamic variables around the moment of minimum bubble radius. A compressional wave starts to form in the velocity profile at the instant t3, and it develops into a steep compressional wave at the instant t4, which lasts for a very short time only. The pressure profile also shows a steep change at the instant t4. Finally the compressional wave is reflected at the instant t5. We conclude that shock waves cannot develop even near the experimental upper threshold of the driving pressure.

Although the compressional wave is steeper compared to that as shown in Fig. 1, the maximum gas density, pressure, and temperature attained are nearly the same. Also, the degrees of ionization are shown in Fig. 6, which is similar to that shown in Fig. 3. Only Ar^+ is the dominant ion (about 30% at the maximum) with a few Ar^{2+} present (below 1%). Therefore, neglecting the sudden increase as it only lasts for a very short time, we estimate the maximum degree of ionization α near the upper threshold of SBSL to be about 30%, which is still much lower than that reported in Ref. [15].

D. Onset of SBSL

We next discuss the situation at the onset of SBSL. We set the driving frequency $f=26.5$ kHz, driving pressure $P_a=1.23$ atm, and ambient radius $R_0=2.2$ μm. The surface tension σ is set to be 0.05 $\mathrm{kg\,s^{-2}}$ in order to fit an experimental $R(t)$ curve [27]. The values of other parameters are the same as before.

Figure 7 shows snapshots of the spatial profiles of the thermodynamic variables around the time when the bubble attains its minimum. Comparing it to Fig. 1, we find that the compressional wave becomes weaker. The compressional wave is associated with a salient drop of temperature in the

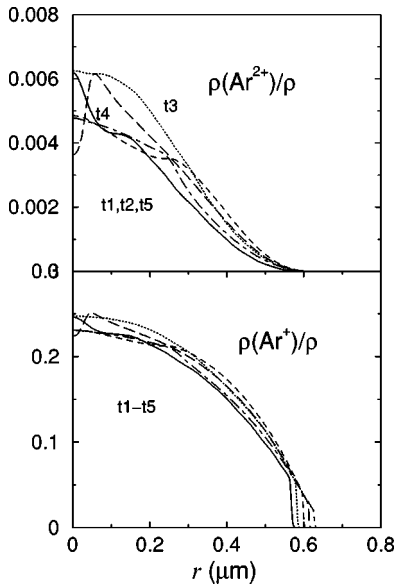

FIG. 6. Snapshots of the spatial profiles of the proportions of Ar^+ and Ar^{2+} for $P_a=1.35$ atm and $R_0=5.4$ μm using MVEOS and RP3. The values of t1, t2, etc., are the same as those in Fig. 5.

ionized inner region. It should be noticed that the spatial profiles are smooth at the instant t1. At this time, the ''ignition temperature'' has not been reached to ignite ionization, as discussed before, and so the profiles are as smooth as those shown in Fig. 2. A pressure wave moves outward from the bubble center at t3, reflecting at the bubble wall between t3 and t4, and goes inward at t4. This motion of the pressure wave produces the multipeak structure of the temperature profiles in Figs. 1, 3, 5, and 7, and the subsequent temperature variations are reflected also in the ionization profiles (Figs. 4 and 11). As the bubble continues to collapse, the temperature is high enough to ignite ionization, and so there is a drop of temperature in the inner region at the instant t2.

The corresponding spatial profiles of the proportions of ions are shown in Fig. 8. As expected, ionization has not

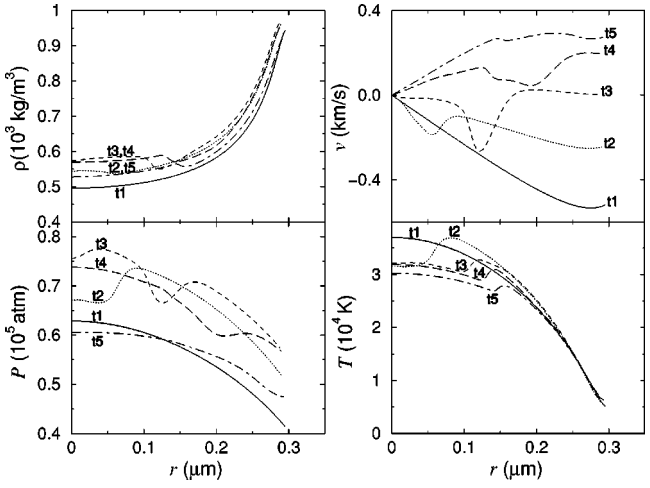

FIG. 7. Same as Fig. 1, but with $P_a=1.23$ atm and $R_0=2.2$ μm. Here, t1$=-28$ ps, t2$=-14$ ps, t3$=-1$ ps, t4 $=12$ ps, and t5$=26$ ps.

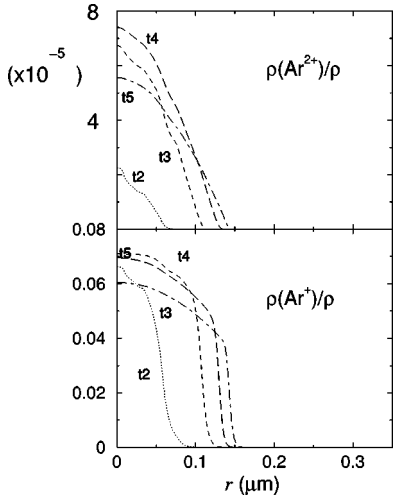

FIG. 8. Snapshots of the spatial profiles of the proportions of Ar^+ and Ar^{2+} for $P_a=1.23$ atm and $R_0=2.2$ μm using MVEOS and RP3. The values of t1, t2, etc., are the same as those in Fig. 7.

started at the instant t1. Even after it has, the density of Ar^+, which is the dominant ion, is greatly reduced to about 7% at the maximum. Second ionization Ar^{2+} is hardly found (less than 10^{-4}). Therefore, the maximum degree of ionization α is only about 7% at the onset of SBSL.

E. Effects of EOS

Since an SL bubble is compressed to a very small volume, it can be sensitive to the treatment of the short-range repulsion of the gas molecules. In the MVEOS (15), this is handled by an ad hoc excluded volume term. Therefore, it is worth using a more realistic EOS, MYEOS (16), for comparison.

We again study the case with $P_a=1.325$ atm and $R_0=4.7$ μm. Figure 9 shows snapshots of the spatial profiles of several thermodynamic variables around the moment of minimum bubble radius, using MYEOS. We notice that a smaller bubble radius $R_{\min}$ (about 0.45 μm) is reached compared to that obtained using MVEOS (about 0.6 μm). This is clearly due to the absence of the excluded volume term in the MYEOS. As a result of the greater compression ratio $(R_{\min}/R_0)$, the gas density and pressure attained are nearly doubled, and a higher temperature of 60 000 K is reached. Although the bubble is compressed to a smaller radius, there is still no shock wave developed. Since the temperature is increased, the proportion of Ar^+ is also increased slightly as shown in Fig. 10. The first ionization Ar^+ contributes about 24% with a few Ar^{2+} present (about 1%). Neglecting the sudden increase as it only lasts for a very short time, we estimate the maximum degree of ionization α to be about 30%.

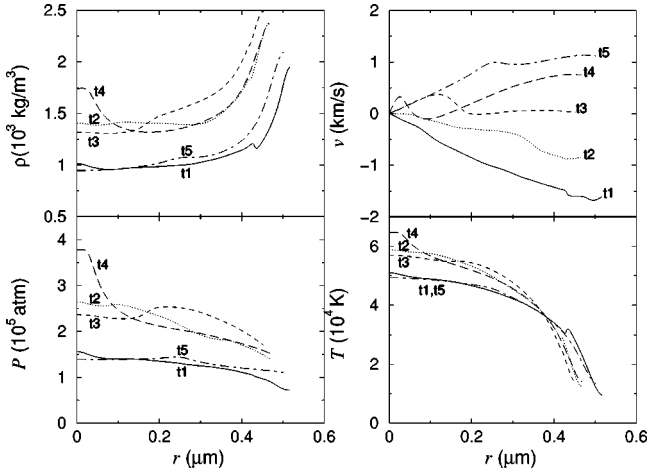

FIG. 9. Same as Fig. 1, but using MYEOS. Here, t1=−72 ps, t2=−33 ps, t3=1 ps, t4=34 ps, and t5=70 ps.

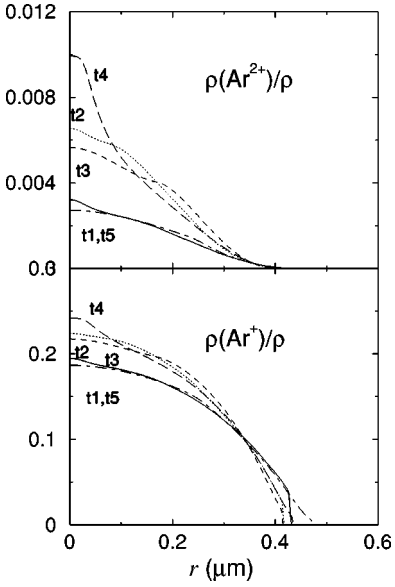

FIG. 10. Snapshots of the spatial profiles of the proportions of Ar^+ and Ar^{2+} for $P_a=1.325$ atm and $R_0=4.7$ μm using MYEOS and RP3. The values of t1, t2, etc., are the same as those in Fig. 9.

The time variations of the temperature and number density of Ar^+ at the bubble center are shown in Fig. 11. The variations are generally the same as those in Fig. 4. The central temperature increases smoothly at first before there is any ionization. It suddenly drops when ionization starts at about $t=-175$ ps; the ''ignition temperature'' is found to be about 43 000 K. The temperature and the Ar^+ density reach local maxima slightly before the time that the bubble attains its minimum radius. A sudden increase in the temperature and the Ar^+ density occurs at $t=30$ ps, which is captured in Figs. 9 and 10 at the instant t4.

Table I summarizes the extreme values attained for the different driving pressures and ambient radii with the two different EOS's used. We find that the minimum bubble radii $R_{\min}$ reached are at least 20% smaller when using MYEOS instead of MVEOS. Besides, the maximum gas densities attained are approximately doubled, while the pressure, temperature, and the Mach number only increase relatively slightly. On average, MYEOS gives a higher degree of ionization for the same driving pressure, except at the sudden increase.

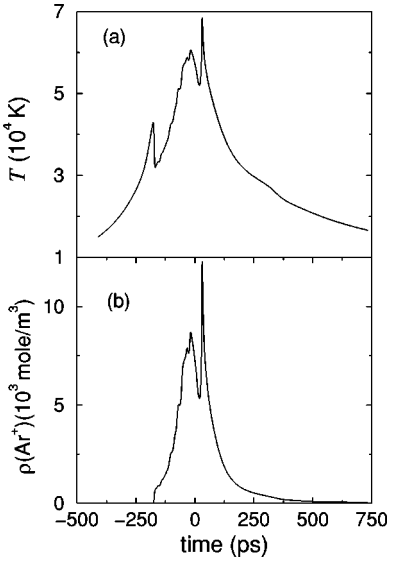

FIG. 11. Same as Fig. 4, but using MYEOS. Here, the bubble attains its minimum radius at $t=0$.

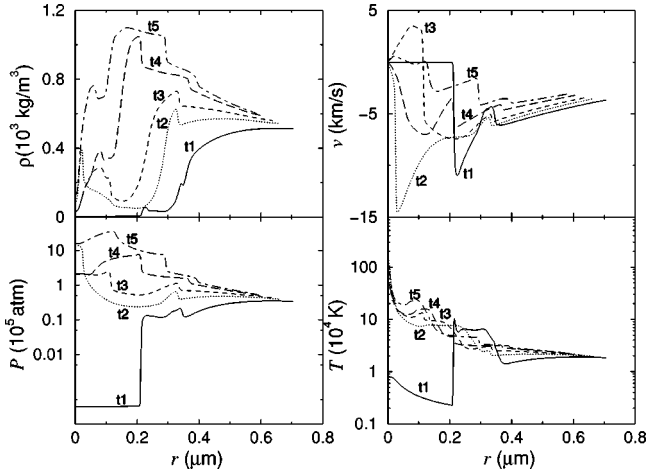

FIG. 12. Same as Fig. 1, but using MVEOS and RP1, and without considering surface tension, heat conductivity, and viscosity. Here, t1 = −51 ps, t2 = −40 ps, t3 = −33 ps, t4 = −23 ps, and t5 = −17 ps.

F. Effects of physical parameters

Yuan *et al.* and Cheng *et al.* have shown that shock waves develop when some physical effects are neglected [21,22]. In order to study the effect of the surface tension, thermal conductivity, water compressibility, and viscosity, a simulation was done with these being neglected. We solve the Euler equations and RP1 instead of the Navier-Stokes equations and RP3, respectively. The parameters and material constants used are the same as those used in Ref. [15] with $P_a = 1.425$ atm and $R_0 = 4.5$ μm.

The results shown in Figs. 12 –14 are significantly different from those obtained by solving the Navier-Stokes equations and RP3, but the results are very similar to those shown in Ref. [15].

As shown in Figs. 12 and 13, we find that a very high temperature up to 10^6 K is reached, and shock waves are formed. A very steep shock wave has already developed at the instant t1, and it propagates toward the center of the bubble. The shock wave reflects out between instants t3–t8, and it is weakened to become a compressional wave propagating inwards again after the instant t9. It was already pointed out in Refs. [21,22] that the use of RP1 makes shock waves more likely to develop, and a very high temperature can be reached due to the absence of thermal conduction.

On the other hand, as shown in Fig. 14, argon atoms are strongly ionized. More argon atoms are ionized near the bubble center; nearly all atoms are ionized to Ar^{5+} within a core of radius 0.05 μm at the bubble center.

G. Calculated pulse widths and spectra

The total power of radiated visible light versus time at different driving pressures is shown in Fig. 15; the solid lines denote the results obtained by the refined blackbody radiation model, and the dashed lines denote the results without absorption. Because of the absorption, the peak power drops by about 33% at $P_a = 1.275$ atm, in which case the degrees of ionization are not very high. As the driving pressure increases, the degrees of ionization increase, and the drop in the peak power becomes more significant. At $P_a = 1.35$ atm, the maximum degree of ionization is about 30% and the peak power drops by about 75%.

TABLE I. Extrema values for argon bubble collapse using different EOS's. Here, ρ_c^{max} is the maximum density at the bubble center, ρ_b^{max} the maximum density at the bubble wall, and P_c^{max} and T_c^{max} are the maximum pressure and temperature, respectively, at the bubble center.

P_a (atm)	EOS	R_{min} (μm)	ρ_c^{max} (kg m^{-3})	ρ_b^{max} (kg m^{-3})	P_c^{max} (10^5 Pa)	T_c^{max} (10^4 K)	$Mach_{max}$
1.275	MVEOS	0.33	710	953	1.7	4.4	1.69
	MYEOS	0.26	1384	1998	2.0	4.8	1.71
1.30	MVEOS	0.50	784	1022	3.0	5.4	1.97
	MYEOS	0.39	1589	2360	3.1	5.9	2.01
1.325	MVEOS	0.59	871	1043	4.9	6.2	2.04
	MYEOS	0.45	1954	2489	4.6	6.8	2.08
1.35	MVEOS	0.68	923	1056	6.9	6.8	2.06
	MYEOS	0.52	2353	2616	7.0	7.9	2.10

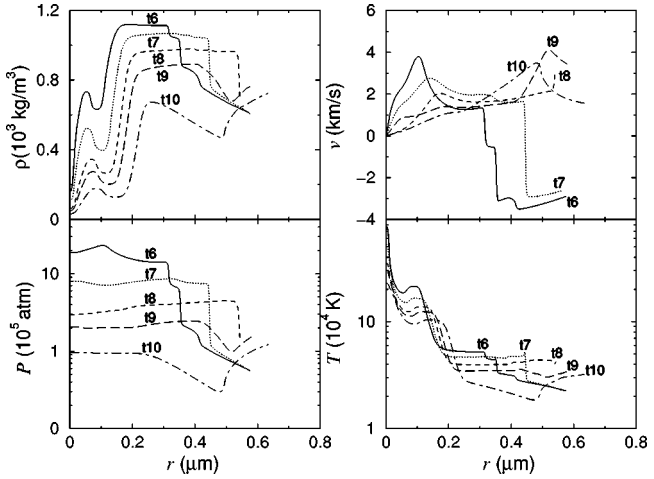

FIG. 13. Same as Fig. 11, but the starting time is t6 with t6 = −13 ps, t7 = −8 ps, t8 = 0 ps, t9 = 9 ps, and t10 = 20 ps.

We find that the peak power and the pulse width are larger at larger driving pressures. The peak power and pulse width increase from about 5 mW and 69 ps to 70 mW and 206 ps as the driving pressure increases within the stable SBSL regime. In the refined model, both the peak power and the pulse widths are comparable to the experimental results [2].

Figure 16 shows the time variations of the normalized blackbody radiation power for ''UV'' (300–400 nm) and ''red'' (590–650 nm) light at various driving pressures. The pulse shapes and widths are very similar in the two wave bands.

The origin of the small drops and the shoulders in the power is the appearing and disappearing of the inner core. The size of the inner core increases very rapidly at first, and this leads to a sudden increase of photon absorption. Therefore, the emitted power drops suddenly. We test this by changing the value of l_λ^{tot}. If the value of l_λ^{tot} is larger, the

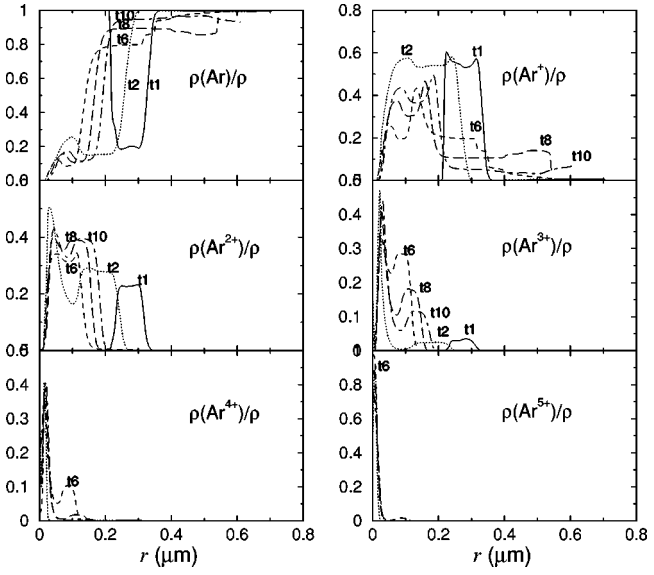

FIG. 14. Snapshots of the spatial profiles of the proportions of the neutral atom and ions for the same condition as that in Figs. 12 and 13. The values of t1, t2, etc. are also the same.

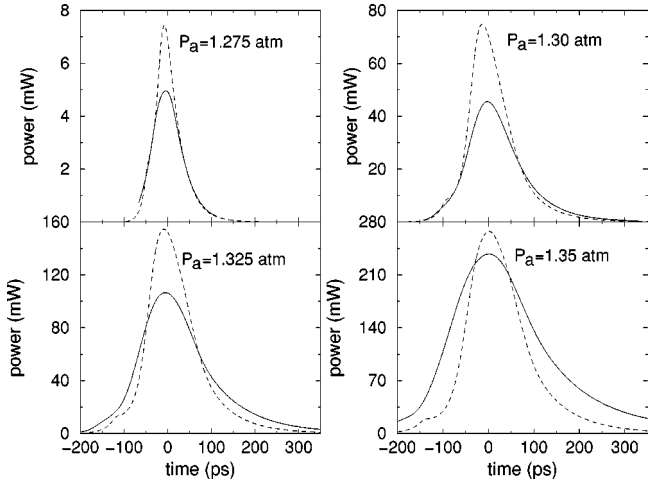

FIG. 15. Blackbody radiation power versus time for different driving pressures. The solid line denotes the power calculated using the refined model, and the dashed line denotes the power without absorption. Here, $t=0$ refers to the time that the bubble attains its minimum radius.

core will appear earlier and disappear later, and so the small drops and the shoulders will be shifted down. However, the overall shapes of the curves and the spectra are not changed significantly by the choice of l_λ^{tot}.

Finally, we compare the calculated spectra with the experimental ones. Figure 17 shows the spectra at different driving pressures averaged over one acoustic cycle. Again, the squares denote the experimental data for Ar taken out from Fig. 56 in Ref. [1]. The shapes of our spectra are very similar to the experimental ones. The spectrum at $P_a = 1.275$ atm is just like the shifted-up spectrum of the experimental one.

The spectra calculated assuming an optically thin bubble are shown in Fig. 18. There are two obvious differences

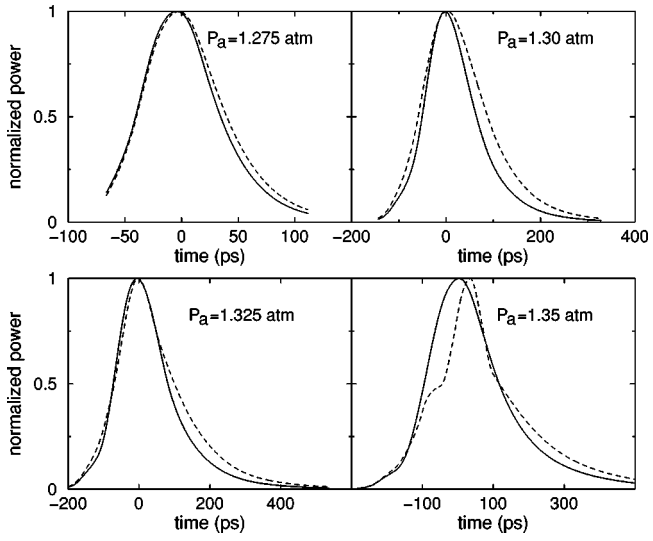

FIG. 16. Normalized refined blackbody radiation power for different parts of the spectrum versus time. The solid line denotes the UV part, and the dashed line denotes the red part. Here, $t=0$ refers to the time that the bubble attains its minimum radius.

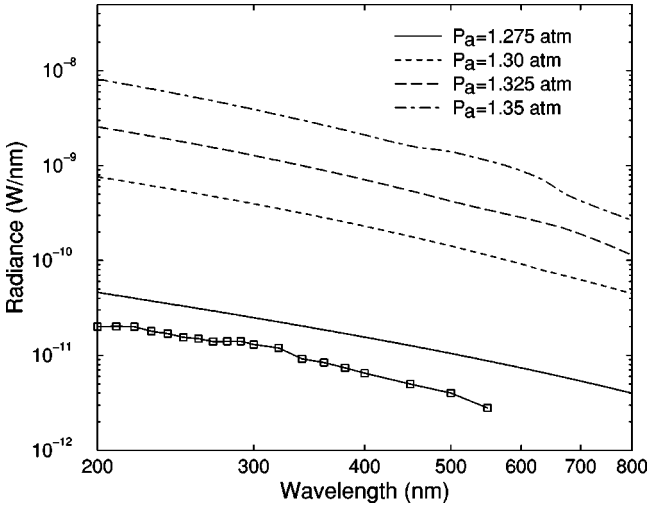

FIG. 17. Refined blackbody radiation spectra at different driving pressures averaged over one acoustic cycle. The squares denote the experimental data for Ar taken out of Fig. 56 in Barber *et al.* [1].

when we compare them to those shown in Fig. 17. First, the spectra are shifted up due to the lack of absorption. The shift up is more significant for large driving pressures, because photon absorption is more important in those cases. Second, the amount of radiation at long wavelengths is increased. This again reveals that red light is absorbed more significantly.

We set $P_a = 1.263$ atm and $R_0 = 2.6$ μm, and the corresponding spectrum, shown in Fig. 19, nicely fits the experimental spectrum. The spectrum calculated without considering absorption is also shown by the dashed line in the same figure. The preferential absorption of red light by the bubble content is important for the agreement between the calculated and the experimental spectra. We caution the readers that a quantitative comparison between the theoretical and experimental spectra cannot be made at this point, because the precise experimental driving pressure is not known. We

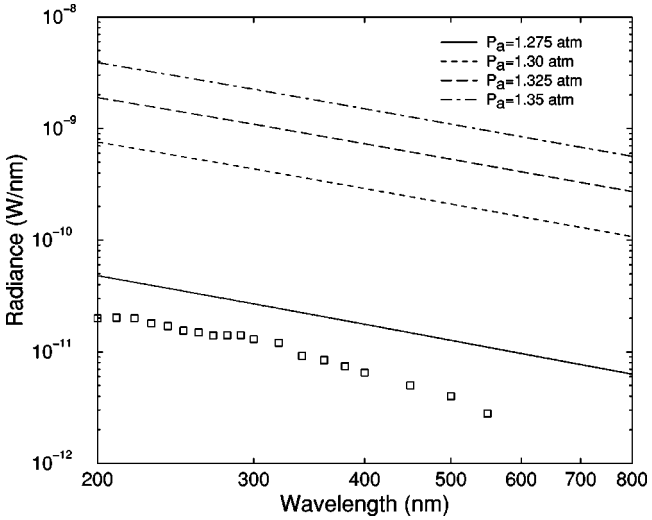

FIG. 18. Same as Fig. 17, but the blackbody radiation spectra calculated ignoring absorption are shown instead.

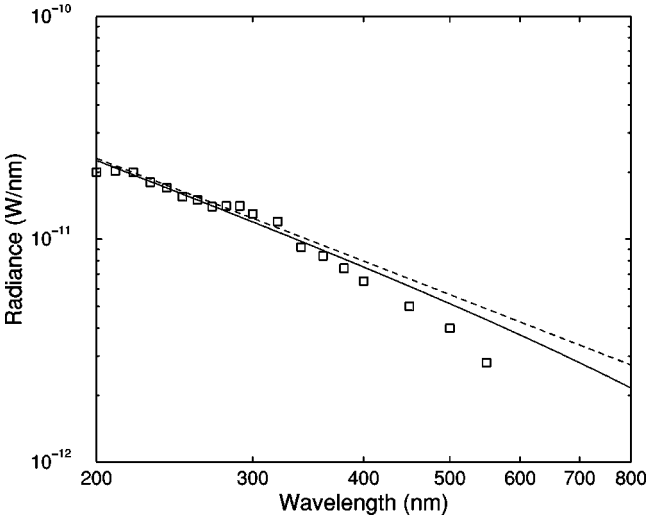

FIG. 19. The squares denote the experimental spectrum for Ar taken out of Fig. 56 in Barber *et al.* [1]. We set $P_a = 1.263$ atm and $R_0 = 2.6$ μm, and the spectrum obtained using the refined model (solid line) nicely fits on the experimental one. The spectrum calculated without considering absorption (dashed line) is also shown for reference.

show Fig. 19 only to show that our refined blackbody model may bring down the magnitude of the red light portion of the spectrum, resulting in a better qualitative agreement with the experimental spectral shape.

V. SUMMARY

We have presented a hydrodynamical framework to study the dynamics of the ionized gas inside an SL bubble. Conservation laws with source terms are solved to monitor the densities of argon atoms, ions, and electrons. We also take into account the processes of collisional ionization, radiative recombination, and three-body recombination.

In the stable SBSL regime, our results indicate that shock waves are absent, and the compressional waves are already strong enough to produce moderate temperature and ionization, which in turn strengthens the compressional waves. This again confirms our view [22] that shock waves are not needed to explain SBSL.

We have shown that the maximum degree of ionization is about 7% near the onset of SBSL and about 30% near the upper threshold of SBSL using MVEOS. Slightly higher degrees of ionization is obtained using MYEOS. The degrees of ionization are much lower than the dramatic multiple ionizations reported by Xu *et al.* [15] but significantly higher than that (below 1%) reported in Refs. [17,28]. The partially ionized core of an SL bubble becomes optically opaque, which bears important consequences on the emitted light.

Finally, we presented a refined blackbody radiation model which takes the finite opacity into account. We model an SL bubble by a ''black'' core and a ''gray'' outer shell and calculate the emitted light accordingly, using the time and radius-dependent mean free path obtained in our hydrodynamics simulation. The resulting peak power, spectra, pulse

widths, and their wavelength dependence all agree with the experimental observations very well.

Several effects not considered here may be important for a realistic simulation of SBSL. We have ignored the presence of water vapors, which may play a role in SBSL [37–39]. We also have not taken into account possible modifications of the various reaction rates due to the high pressure at SBSL condition. Another high-pressure effect that we have left out is the possibility of solidification of air, which may lead to a substantial change of the EOS.

The basic blackbody light emission model is inadequate for SBSL because it gives rise to a larger pulse width for red light than blue light. This is because the bubble interior reaches a temperature high enough to emit blue light only during a short duration compared to that for red light emission. This problem is solved in our calculation by taking into account the wavelength-dependent absorption in the outer shells, thereby suppressing the width of the red light pulse preferentially.

We do not find a drastic degree of ionization in an SL bubble, and hence we do not expect the presence of a large electric field such as reported by Xu *et al.* [16]. Our results indicate that the bubble interior is relatively mild and uniform, and large temperature or electric-field gradients are easily smoothed out when more realistic physical processes are considered. In particular, the presence of water vapors is known to bring a significant cooling of the bubble interior [37–39]. The degree of ionization in an SL bubble will likely be even lower when processes not considered here, such as aspherical deformation and evaporation/condensation [37–39], are included.

ACKNOWLEDGMENTS

We are grateful for the support of a Hong Kong Research Grants Council Grant No. CUHK 312/96P and a Chinese University Direct Grant (Project ID: 2060093). L.Y. is also supported by the National Key program for developing basic sciences (G1999032801).

[1] B. P. Barber, R. A. Hiller, R. Löfstedt, S. J. Putterman, and K. R. Weninger, Phys. Rep. **281**, 65 (1997).
[2] B. Gompf, R. Günther, G. Nick, R. Pecha, and W. Eisenmenger, Phys. Rev. Lett. **79**, 1405 (1997).
[3] R. A. Hiller, S. J. Putterman, and K. R. Weninger, Phys. Rev. Lett. **80**, 1090 (1998).
[4] M. J. Moran and D. Sweider, Phys. Rev. Lett. **80**, 4987 (1998).
[5] B. Noltingk and E. Neppiras, Proc. R. Soc. London, Ser. B **63**, 674 (1950).
[6] P. Jarman, J. Acoust. Soc. Am. **32**, 1459 (1960).
[7] C. C. Wu and P. H. Roberts, Phys. Rev. Lett. **70**, 3424 (1993).
[8] W. Moss *et al.*, Phys. Fluids **6**, 2979 (1994).
[9] W. Moss, D. B. Clarke, and D. A. Young, Science **276**, 1398 (1997).
[10] W. Moss *et al.*, Phys. Rev. E **59**, 2986 (1999).
[11] L. Frommhold and A. A. Atchley, Phys. Rev. Lett. **73**, 2883 (1994).
[12] L. Frommhold, Phys. Rev. E **58**, 1899 (1998).
[13] C. Eberlein, Phys. Rev. Lett. **76**, 3842 (1996).
[14] L. S. Bernstein and M. R. Zakin, J. Phys. Chem. **99**, 14 619 (1995).
[15] N. Xu, L. Wang, and X. Hu, Phys. Rev. E **57**, 1615 (1998).
[16] N. Xu, L. Wang, and X. Hu, Phys. Rev. Lett. **83**, 2441 (1999). We note that the units used in the reaction rates in this reference are contradictory to those in Ref. [13], especially the recombination rate. We adopt the formulas in Ref. [13].
[17] S. Hilgenfeldt, S. Grossmann, and D. Lohse, Nature (London) **398**, 402 (1999).
[18] V. Q. Vuong and A. J. Szeri, Phys. Fluids **8**, 2354 (1996).
[19] V. Q. Vuong, A. J. Szeri, and D. A. Young, Phys. Fluids **11**, 10 (1999).
[20] M.-C. Chu and D. Leung, J. Phys.: Condens. Matter **9**, 3387 (1997).
[21] L. Yuan, H. Y. Cheng, M.-C. Chu, and P. T. Leung, Phys. Rev. E **57**, 4265 (1998).
[22] H. Y. Cheng, M.-C. Chu, P. T. Leung, and L. Yuan, Phys. Rev. E **58**, R2705 (1998).
[23] Lord Rayleigh, Philos. Mag. **34**, 94 (1917).
[24] M. Plesset, J. Appl. Mech. **16**, 277 (1949).
[25] V. Kamath and A. Prosperetti, J. Acoust. Soc. Am. **85**, 1538 (1987).
[26] A. Prosperetti and A. Lezzi, J. Fluid Mech. **168**, 457 (1986).
[27] D. F. Gaitan, L. A. Crum, R. A. Roy, and C. C. Church, J. Acoust. Soc. Am. **91**, 3166 (1992).
[28] S. Hilgenfeldt, S. Grossmann, and D. Lohse, Phys. Fluids **11**, 1318 (1999).
[29] Y. B. Zeldovich and Y. P. Raizer, *Physics of Shock Waves and High-Temperature Hydrodynamic Phenomena*, edited by W. D. Hayes and R. F. Probstein (Academic Press, New York, 1966), Vol. I.
[30] C. Y. Ho, L. Yuan, M.-C. Chu, P. T. Leung, and W. Wei, Europhys. Lett. **56**, 891 (2001).
[31] T. W. Chen, P. T. Leung, and M.-C. Chu, Phys. Rev. E **62**, 6584 (2000).
[32] B. P. Barber, C. C. Wu, R. Löfstedt, P. H. Roberts, and S. J. Putterman, Phys. Rev. Lett. **72**, 1380 (1994).
[33] S. Hilgenfeldt, D. Lohse, and M. P. Brenner, Phys. Fluids **8**, 2808 (1996).
[34] S. Hilgenfeldt, D. Lohse, and W. C. Moss, Phys. Rev. Lett. **80**, 1332 (1998).
[35] H. C. Yee (unpublished).
[36] W. S. Don and C. B. Quillen, J. Comput. Phys. **122**, 244 (1995).
[37] B. D. Storey and A. J. Szeri, Proc. R. Soc. London, Ser. A **456**, 1685 (2000).
[38] K. Yasui, Phys. Rev. E **56**, 6750 (1997); **60**, 1754 (1999).
[39] R. Tögel, B. Gompf, R. Pecha, and D. Lohse, Phys. Rev. Lett. **85**, 3165 (2000).